J. Fluid Mech. (2001), *vol.* 439, *pp.* 335–352. Printed in the United Kingdom

Sound production of vortex–nozzle interactions

By S. J. HULSHOFF[1], A. HIRSCHBERG[2] AND G. C. J. HOFMANS[2]

[1]Faculty of Aerospace Engineering, Delft University of Technology, The Netherlands
[2]Department of Physics, University of Eindhoven, The Netherlands

(Received 2 February 2000 and in revised form 29 December 2000)

The factors which affect the sound production of a vortex as it passes through a nozzle are investigated at both low and high Mach numbers using time-accurate inviscid-flow computations. Vortex circulation, initial position, and mean-flow Mach number are shown to be the primary factors which influence the amplitude and phase of the sound produced. Nozzle geometry and distribution of vorticity are also shown to play significant roles in determining the detailed form of the signal. Additionally, it is shown that solution bifurcations are possible at sufficiently large values of vortex circulation. Comparisons are made between sound signals computed directly using a numerical method for the Euler equations and predictions obtained using a compressible vortex-sound analogy coupled with a compact-source assumption for the computation of vorticity dynamics. The results confirm that the latter approach is accurate for a range of problems with low mean-flow Mach numbers. At higher Mach numbers, however, the non-compactness of the source becomes apparent, resulting in significant changes to the character of the signal which cannot be predicted using the analogy-based approach. Implications for the construction of simplified models of vortex sound in solid-rocket nozzles are discussed.

1. Introduction

Sound production due to vortex–nozzle interactions has been recently identified as a potential source for the large-amplitude low-frequency pulsations observed in solid-rocket motors (Dunlap & Brown 1981; Dotson, Koshigoe & Pace 1997; Vuillot 1995). Solid-rocket flows are very complex, as they include combustion, entrained solid phases, and time-variant geometries. There is therefore considerable motivation to develop simplified models of the processes contributing to the pulsations. Most of a rocket-nozzle flow is subsonic, motivating attempts (see Hirschberg *et al.* 1998) to model the contribution of vortex–nozzle sound production using the incompressible vortex-sound theory of Powell (1964), or the compressible counterpart developed by Howe (1975*b*). For both approaches a compact-source assumption may be employed, allowing the vorticity dynamics to be efficiently computed using an incompressible description of the flow. As the throat of a solid-rocket nozzle operates at sonic conditions, however, it is not clear to what extent vortex-sound theory can be used to adequately describe the most important elements of vortex–nozzle sound production.

In this paper we will examine vortex–nozzle sound production in detail, using the results of numerical simulations. The goal is to investigate the influence of vortex position and strength, nozzle geometry, and the effects of compressibility, in order to

gauge their relative importance for the construction of approximate models. A number of authors have considered similar problems using analytic techniques (Flandro 1986; Dunne & Howe 1997) and numerical techniques suitable for low Mach number flows (Conlisk & Rockwell 1981; Hourigan, Welsh & Thompson 1990; Thompson, Hourigan & Welsh 1992). Here we examine the range of application of low Mach number approximations by comparison with more general numerical solutions.

In the first part of the paper, the parameters influencing vortex–nozzle sound at low Mach numbers are investigated using a vortex-blob potential-flow technique combined with the acoustic analogy developed by Howe (see Howe 1975*a*, *b*). In the second part, a numerical solution procedure for the full Euler equations is used to investigate the influence of compressibility.

The nozzle geometries considered are two-dimensional, corresponding to experimental models which have been used to study vortex–nozzle interactions in the absence of combustion (Couton *et al.* 1998). These are planar in geometry for improved optical access. We also consider only monotonically converging nozzles, without additional cavities in the inlet region. This limits the possible influence of flow separations which may occur from smooth portions of the nozzle walls. For the relatively high Reynolds numbers of interest, the location and details of such separations are very difficult to predict. In contrast, for rectangular nozzle geometries it is possible to specify a separation point at the sharp edge of the nozzle inlet. When the vortex blob method is used, this could be done using a single vortex at the sharp edge, as proposed by Brown & Micheal (1954). This idea has been used in aero-acoustics by Howe (1975*b*, 1998) and Peters (1993). In view of the uncertainties present in such models, however, we limit ourselves to the consideration of the purely inviscid sound-production effects present for all geometries considered in this study.

The monotonically converging nozzles considered here are in contrast to some integrated nozzle designs appearing in solid-rocket motors, which have an additional cavity in the area near the inlet. Recently, Anthoine, Buchlin & Guery (2000) have demonstrated that such cavities act to increase the level of sound production. This may be explained in terms of vortex-sound theory, which predicts an increase roughly proportional to the volume of the cavity, corresponding to the scaling law for the acoustical velocity at the vortex path. We consider here the limit case of zero cavity volume, which therefore corresponds to nozzle designs which have minimum sound production.

2. Vortex–nozzle sound at low Mach numbers

Figure 1 illustrates the basic geometry of a vortex–nozzle interaction. A distribution of vorticity, with an initial mean height of h, is convected past a nozzle separating two sections of channel with heights S_1 and S_2. The channels are assumed to be of infinite length, so that both the upstream and downstream conditions are anechoic. Sound production occurs due to interaction of the vortex with the change in geometry, and acoustic waves p^- and p^+ are radiated upstream and downstream. For low Mach number flows, we first investigate the problem using a vortex-blob potential-flow solution procedure originally developed by Krasny (1987) (see also Hofmans 1998; Graziani, Ranucci & Piva 1995; Peters 1993), coupled with the acoustic analogy derived by Howe. A number of different conditions are considered in order to investigate the effects of nozzle geometry and vorticity strength and distribution. To simplify the discussion, we will limit our attention to the upstream-travelling wave,

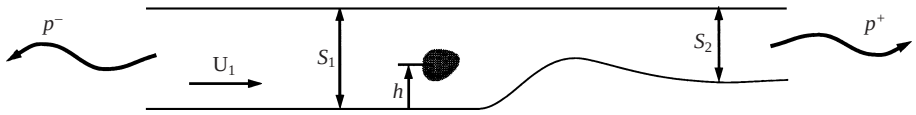

FIGURE 1. Vortex convection through a nozzle.

p^-, and to negative vortex circulations. In a solid-rocket motor, the vortex circulations generated are negative in sign, and it is the p^- wave which drives the instability.

2.1. *Acoustic analogy*

For sufficiently low Mach numbers, the sound production region near the geometric change may be assumed to be compact. It is then possible to derive analytic expressions for p^-. This problem has been considered by Howe (1975*b*), who derived expressions for perturbations due the convection of both entropic and vortical inhomogeneities in internal flows with changes in cross-sectional area. Howe's analogy is based on Crocco's relation:

$$\frac{\partial \boldsymbol{v}}{\partial t} + \nabla B = -\boldsymbol{\omega} \times \boldsymbol{v} + T\nabla s \tag{2.1}$$

where $\boldsymbol{v}$ is the total velocity vector, B is the total enthalpy, $\boldsymbol{\omega}$ is the vorticity vector, and T and s are the local values of temperature and entropy. Combining this equation with the mass conservation law:

$$\frac{1}{\rho}\frac{\mathrm{D}\rho}{\mathrm{D}t} = -\nabla \cdot \boldsymbol{v} \tag{2.2}$$

where ρ is the local density and $\mathrm{D}/\mathrm{D}t = \partial/\partial t + \boldsymbol{v} \cdot \nabla$, the following exact non-homogeneous equation can be obtained:

$$\frac{1}{c^2}\frac{\mathrm{D}_o^2 B}{\mathrm{D}t^2} - \nabla^2 B = \nabla \cdot (\boldsymbol{\omega} \times \boldsymbol{v} - T\nabla S) + \left(\frac{1}{c_o^2}\frac{\mathrm{D}_o^2 B}{\mathrm{D}t^2} - \frac{\partial}{\partial t}\left(\frac{1}{c^2}\frac{\mathrm{D}i}{\mathrm{D}t}\right)\right) \tag{2.3}$$

where for an isentropic flow, $\mathrm{D}S/\mathrm{D}t = 0$. Here i is the local value of enthalpy, c_o is the speed of sound of a mean flow which has a value $\boldsymbol{U}$ for the steady part of its potential-flow component of the velocity, and $\mathrm{D}_o/\mathrm{D}t = \partial/\partial t + \boldsymbol{U} \cdot \nabla$ corresponds to that mean flow. Howe's analogy (2.3) is still exact within the inviscid, isentropic flow assumption. We can interpret the right-hand side of this equation as sources of sound as heard by a listener immersed in the uniform reference flow. Like Lighthill's analogy, this expression requires approximation in order to be more tractable than the original governing equations. For low Mach numbers ($M < 0.3$), the second term in the source appears to be negligible (see Howe 1998). We will further assume that the source region is compact, which in combination with an assumed simple-wave region far upstream in the channel, allows the use of Howe's low-frequency Green function. The use of such an integral formulation, similar to the case of Lighthill's analogy (Lighthill 1954), is a crucial beneficial step, as it smooths out errors in the evaluation of the source term.

By using the reverse-flow theorem (Howe 1975*b*), it is possible to derive expressions for far-field total enthalpy perturbations based on the convolution of a low-frequency approximation to the Green's function. For regions far upstream of the nozzle, the total enthalpy perturbation may be expressed as

$$B^- = \frac{S_2}{S_1(S_1 + S_2)(1 - M_2)} \cdot \int_V [(\boldsymbol{\omega} \times \boldsymbol{v} - T\nabla s) \cdot \nabla \phi^*] \, \mathrm{d}V \tag{2.4}$$

where ϕ^* is the velocity potential of the irrotational flow associated with the acoustic perturbation (normalized so that $\nabla\phi^* = 1$ far upstream), V is a volume enclosing the source region, M_2 is the downstream Mach number, and the quantities within the square brackets are evaluated at a retarded time proportional to the distance between the source and the far-field point at which the perturbation is measured. For small changes of enthalpy in the upstream region

$$B^- = \frac{p^-}{\rho_o}(1 - M_1) + O(M^2) \tag{2.5}$$

where M_1 is the upstream Mach number. For a homoentropic flow, the upstream pressure perturbation may then be expressed as

$$p_1^- = \frac{S_2}{S_1(S_1 + S_2)(1 - M_1)(1 - M_2)} \cdot \int_V \rho_o[(\boldsymbol{\omega} \times \boldsymbol{v}) \cdot \nabla\phi^*] \, \mathrm{d}V. \tag{2.6}$$

This illustrates that for the low Mach numbers which allow the source region to be described as compact, the acoustic perturbation is directly proportional to the strength of the Lamb vector, $\boldsymbol{\omega} \times \boldsymbol{v}$. There is also a significant amplitude dependence on the Mach numbers characterizing the mean flow.

Expression (2.6) forms an acoustic analogy for the upstream pressure perturbation history in terms of the vorticity dynamics within the source region. It corresponds to a generalization of the Powell analogy (Powell 1964) from stagnant free-field reference conditions to confined uniform-flow reference conditions. As variations of density in the source region have been neglected, however, the level of approximation is similar to that of Powell's analogy. We therefore refer to (2.6) as the Powell–Howe analogy. Although attractive for its simplicity, the range of validity of this approach is unclear, and could be very limited. This will be explored by comparisons with the full Euler method in later sections.

2.2. *Vortex-blob method*

For low Mach numbers, the vorticity dynamics of the source are computed using a vortex-blob method. The vortex-blob method used here is based on a singularity-distribution approach for the solution of plane potential flows. The boundaries of the domain are discretized using piecewise-constant vorticity and source distributions, the strengths of the latter being determined by the local specified normal velocity. In the interior of the domain, the vorticity of the flow is represented using a fixed number of point vortices. Instantaneous velocity fields are computed by the application of a Dirichlet condition on the potentials just outside each panel used to discretize the boundaries of the domain. The positions of the interior point vortices are advanced in time using a fourth-order Runge–Kutta technique, in which the flow velocities are continually updated. In order to prevent erratic movement of point vortices in close proximity to each other, the induced velocity field of each vortex is de-singularized during the position update calculation, as described in Krasny (1987).

2.3. *Results*

For low Mach numbers, the differences in the retarded time of the terms within the square brackets of (2.6) are small. The influence of the inflow and outflow Mach numbers may then be taken into account in terms of factors which scale the pressure perturbation of the $M = 0$ limit. For this section, we thus restrict our attention to $M = 0$ mean flows, and focus on the effects of vorticity distribution and nozzle geometry.

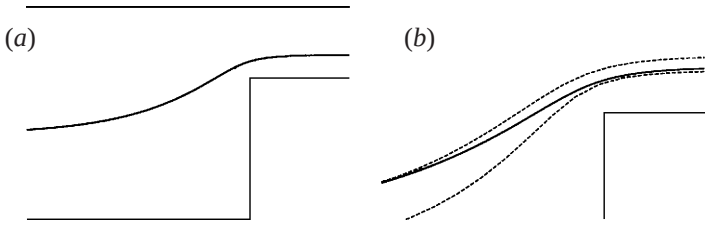

FIGURE 2. Overview of the vortex trajectory (*a*), and magnified comparison of the trajectory (solid) with the irrotational mean flow streamlines (dashed) (*b*).

The most simplified representation of the problem is that of a point vortex interacting with a square nozzle geometry. Figure 2 shows the trajectory computed with the vortex-blob method for a point vortex with circulation $\Gamma = -1.2$ (non-dimensionalized by $U_1 S_1$) interacting with a rectangular nozzle with an area ratio of 3.0. Such values are similar to those encountered in the Ariane V solid rocket motor at the beginning of combustion. A magnified view of the vortex trajectory is compared with two streamlines from the steady irrotational potential flow case in figure 2(*b*). During the approach, the trajectory of the vortex begins to deviate from the irrotational-flow streamlines as it is increasingly influenced by its image system located behind the nozzle walls. The deviation reaches a maximum just behind the entrance to the nozzle, and after a slight decrease, remains at a constant value as the vortex proceeds downstream. The resulting upstream pressure perturbation time history is shown in figure 3 (time non-dimensionalized by S_1/U_1, change in pressure by $\frac{1}{2}\rho_1 U_1^2$). A negative pressure perturbation of increasing magnitude is created as the vortex approaches the vertical wall, which transitions quickly to a positive perturbation as the vortex passes above it. As illustrated in figure 4, this behaviour can be anticipated from (2.6). As the point vortex approaches, its deviation from the irrotational streamlines produces a clockwise rotation of $\boldsymbol{\omega} \times \boldsymbol{v}$, resulting in a component opposing the local irrotational velocity, leading to a negative upstream pressure perturbation. This situation is reversed as vortex passes above the vertical wall. In figure 5 the details of the pressure spike are shown for different time steps and for different numbers of surface panels. The relatively small variation between the various discretizations indicates that the numerical errors associated with the potential-flow solution technique are reasonably small.

Pressure perturbations computed for different initial vortex positions are compared in figure 6. The parameter h is measured from the lower wall, and is non-dimensionalised by the inflow channel height, S_1. As the initial position approaches the lower wall of the geometry, the signal is observed to be delayed, owing to the increasing influence of the image vortex below the wall. Note that the influence of the lower-wall image vortex does not increase sound production in the upstream portion of the flow, as its induction is parallel to the irrotational velocity field. As the vortex approaches the nozzle, however, its sound production is increased relative to the cases with higher initial vortex position. This is due to the increased proximity with which the vortex approaches the corner of the nozzle inlet. Not only are the irrotational velocity gradients higher as the corner is approached, but the image vortex system gains increasing influence over the vortex path. These two factors produce pressure perturbation amplitudes which increase nonlinearly with decreasing initial vortex height.

An effect similar to that obtained by lowering the initial vortex position is obtained

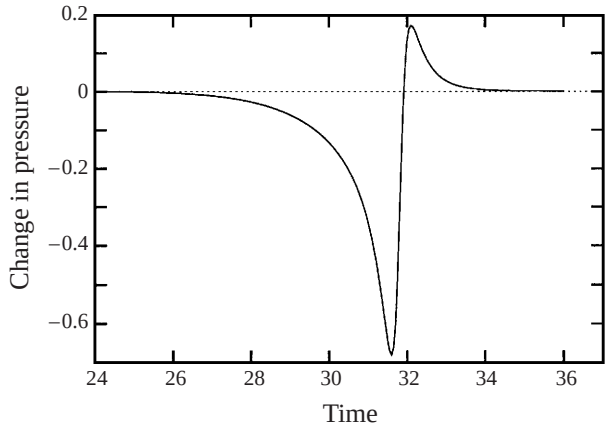

FIGURE 3. Upstream pressure perturbation computed with the vortex-blob technique ($S_1/S_2 = 3$, $\Gamma = -1.2$, $h = 0.4$).

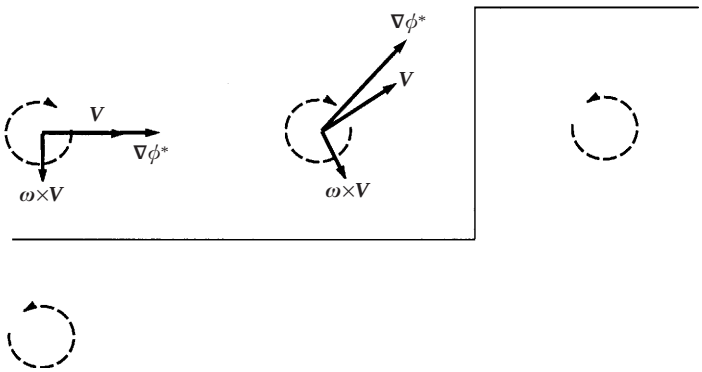

FIGURE 4. The varying terms of (2.6) for a point vortex of negative circulation approaching a wall.

by increasing the vortex circulation. In this case, increases in signal delay are also obtained, along with far larger changes in the magnitude of the pressure perturbation (figure 7). The latter implies a significant increase in vortex-path deviation from the irrotational streamlines due to the image vortex system.

The effects of changing vortex position and circulation are accentuated when the inflow of the nozzle is increased in size. Computations for a square nozzle with $S_1/S_2 = 11.7$ for various values of vortex circulation are shown in figure 8 (this value corresponds to the largest S_1/S_2 for the combustion chamber of the Ariane V solid-rocket motor, occurring near the end of the combustion cycle). The sharpness of the pressure perturbation increases with increasing vortex circulation, until a value is reached at which the vortex fails to exit the domain (figure 9), due to the dominating effect of its image system.

The increasing sharpness of the pressure perturbation signal as the corner is approached is directly related to the singular pressure field associated with the geometric discontinuity. This tends to bias the power of the signal towards higher frequencies. The signal from a rounded $S_1/S_2 = 3$ nozzle with a geometric expansion after the throat (figure 10) is shown for three values of vortex circulation in in figure 11. In addition to an increased characteristic time for the signal, the negative

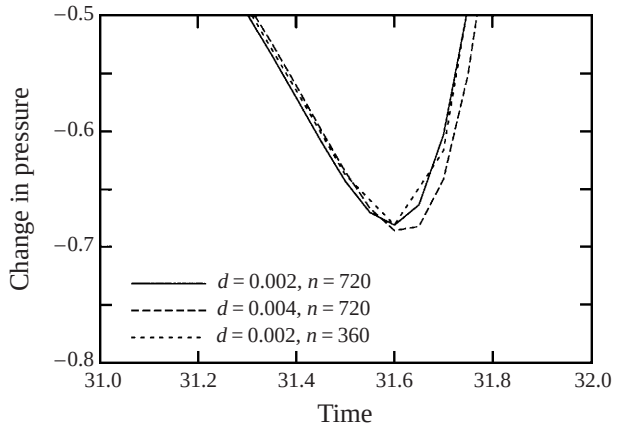

FIGURE 5. Details of the pressure minimum for varying levels of spatial and temporal discretization (d = ratio of corner panel size to throat, n = number of time steps, $S_1/S_2 = 3$, $\Gamma = -1.2$, $h = 0.4$).

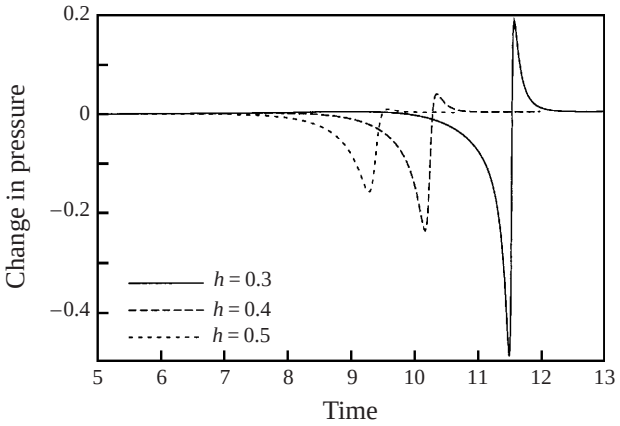

FIGURE 6. Upstream pressure perturbations for varying initial vortex heights ($S_1/S_2 = 3$, $\Gamma = -0.8$, vortex-blob method, equation (2.6)).

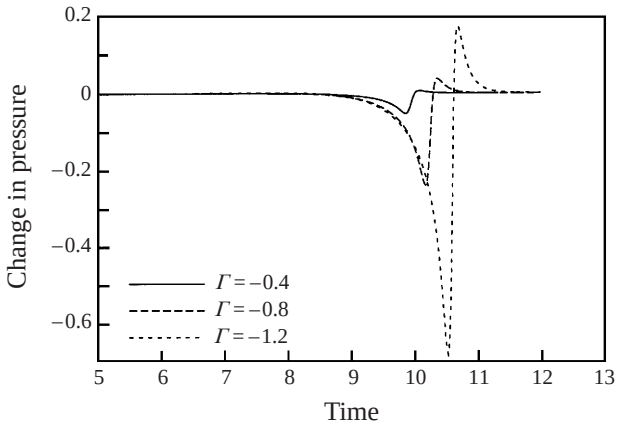

FIGURE 7. Upstream pressure perturbations for varying vortex strengths ($S_1/S_2 = 3, h = 0.4$, equation (2.6)).

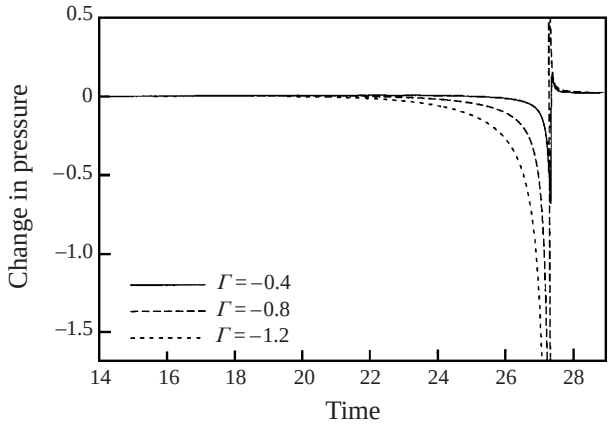

FIGURE 8. Upstream pressure perturbations for varying vortex strengths ($S_1/S_2 = 11.7$, $h = 0.5$, equation (2.6)).

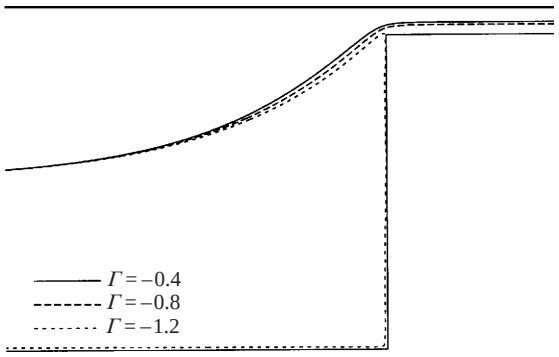

FIGURE 9. Vortex trajectories for varying vortex strengths ($S_1/S_2 = 11.7$, $h = 0.5$, equation (2.6)).

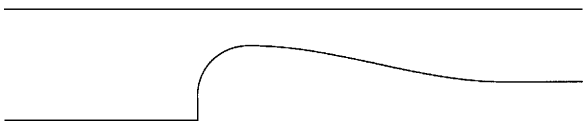

FIGURE 10. Rounded $S_1/S_2 = 3$ nozzle geometry.

pressure peaks and their rate of increase with circulation are attenuated. The positive pressure peak is also of longer duration owing to the slow expansion after the throat.

The final effect considered with the low-Mach-number model is that of distributed vorticity. Figure 12 compares a single-vortex pressure trajectory with that of a distribution of vortices of equivalent total circulation. The distribution was initially circular in shape, with approximately equal spacing between vortices and a centre of vorticity initially at the same initial position as the point vortex. The cloud of distributed vortices is seen to deform as the nozzle is approached, and stretch considerably as it passes through the throat. After the throat, the stretched cloud rotates and deforms about its convecting centre of vorticity. The pressure perturbations of the single- and multiple-vortex computations are compared in figure 13. In spite of its simplified behaviour, the point vortex is seen to provide a fair approximation to the sound generated by a patch of more distributed vorticity.

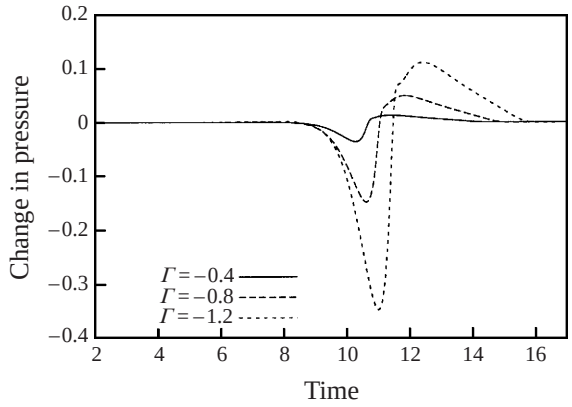

FIGURE 11. Upstream pressure perturbations for the rounded geometry ($S_1/S_2 = 3$, rounded, $h = 0.4$, equation (2.6)).

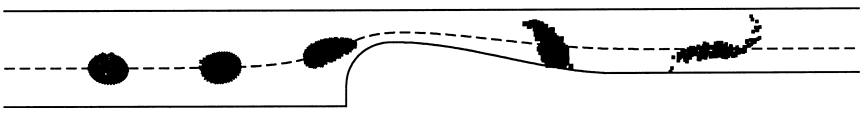

FIGURE 12. Trajectory of a single vortex (solid line) compared with an equivalent cloud of vortices at $t = 10, 20, 30, 40, 50$ (from left to right).

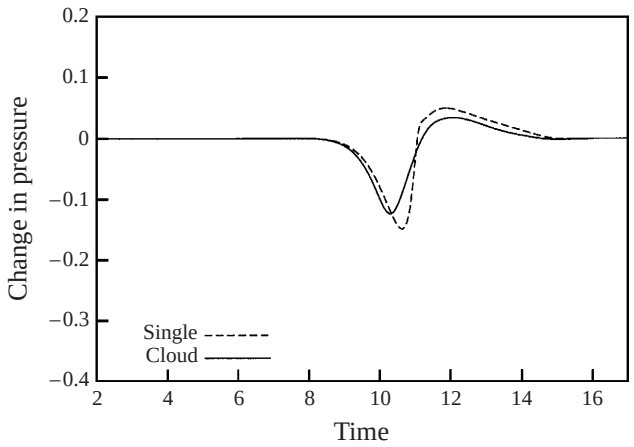

FIGURE 13. Upstream pressure perturbations for the single and equivalent cloud of vortices ($S_1/S_2 = 3$, rounded, $h = 0.4$, $\Gamma = -0.8$ equation (2.6)).

3. Vortex–nozzle sound at higher Mach numbers

In many internal flow applications, the flow Mach numbers, particularly in the region of the nozzle, can be relatively high. For such cases, the assumptions on which the methods of the previous section are based break down. The source region may no longer be considered compact, and variation of relative time delays may become significant for distributed regions of vorticity. In addition, the effects of compressibility can substantially alter the influence of the main flow.

To investigate these effects, a time-accurate numerical procedure for the Euler equations was employed. This technique allows an accurate representation of non-

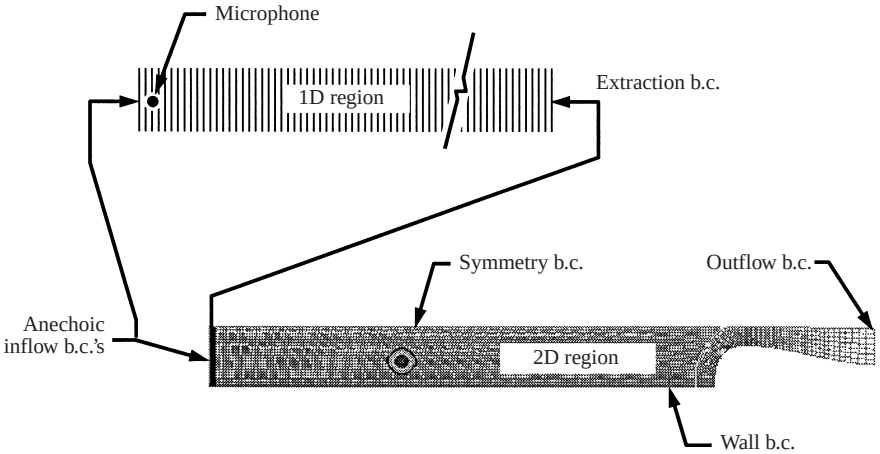

FIGURE 14. Overview of the numerical domain for the Euler computations.

compact sources and mean-flow compressibility, as well as allowing the acoustic perturbations to be measured directly.

3.1. *Euler method*

The time-accurate Euler computations were performed in the numerical domain illustrated in figure 14. The spatial discretization of the Euler equations was based on a two-dimensional, second-order-accurate finite-volume method with scalar nonlinear artificial dissipation (Hulshoff, Hoeijmakers & Mulder 1996). Time integration was performed using an explicit Runge–Kutta technique. The conditions described in Thompson (1987, 1990) were used to maintain anechoic conditions at the inflow and outflow boundaries. For choked conditions, the anechoic outflow boundary condition was replaced by the variable incoming-wave strength conditions described by Poinsot & Lele (1992), configured to maintain a constant exit pressure.

In order to assess the effects of discretization errors on the numerical solutions, computations were performed on both coarse- and fine-mesh discretizations of the domain. The fine mesh had 329 nodes in the streamwise direction and 89 nodes in the normal direction for the first block (located upstream of the nozzle), and 465 nodes in the streamwise direction and 33 normal nodes for the second block (containing the nozzle and exit regions). The coarse mesh was generated with a refinement pattern similar to that of the fine mesh, but with the number of nodes reduced by factors of two in both directions.

To determine the far-field upstream plane-wave response while limiting the extent of the two-dimensional domain, an additional one-dimensional domain was used. This was driven by a flux-conservative extraction from the inflow area of the two-dimensional domain. The extraction was entirely passive, in that the two-dimensional interior solution and its anechoic inflow boundary condition remained unaffected by the procedure. The consistency of this approach was verified using calculations with different extraction positions.

3.2. *Initial vorticity distribution*

The vortices used for the simulations were generated in the inflow region of the two-dimensional domain by the application of a radially symmetric body-force field, centred about a point travelling with the main flow velocity. The spatial distribution

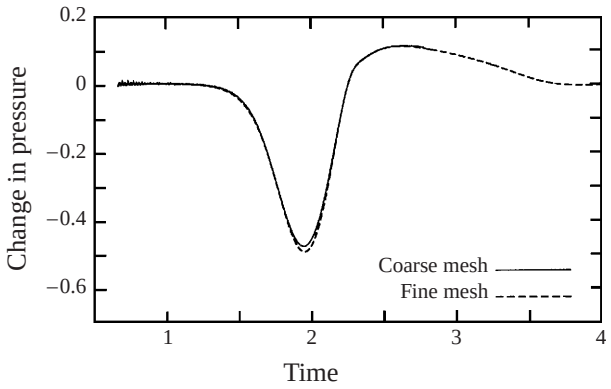

FIGURE 15. Upstream pressure perturbations computed directly with the Euler method on the fine and coarse meshes ($M_1 = 0.01$, $\Gamma = -1.5$, $h = 0.4$).

used was similar to that of the velocity field of a de-singularized incompressible vortex. The body-force field was applied gradually in time, in order to minimize excitation of transverse channel modes. A source term was also added to the energy equation, with a local strength continually updated based on local deviations from homoentropic flow. This prevented the generation of significant entropy gradients resulting from numerical truncation errors within the high-gradient core region. After completion of the vortex generation process, all the source terms were turned off to prevent corruption of the vortex–nozzle interaction signal. In general, the generation procedure provided consistent vortices, although the details of the core vorticity distribution varied with the chosen vortex position and main flow Mach number.

In order to perform comparisons with results from the vortex-blob technique, the vorticity distributions generated with the Euler method were also converted into equivalent point-vortex distributions. This was done by computing local values of circulation within control volumes defined using cells from the Euler mesh and assigning them vortices placed at averaged positions. To avoid the numerical difficulties associated with large numbers of closely spaced vortices, groups of cells were used per control volume, and point vortices were only defined when the circulation exceeded a threshold value. The final circulations of the resulting point vortices were corrected so that their total circulation was equivalent to that of the Euler vorticity distribution.

3.3. *Validation at low Mach numbers*

Upstream pressure time histories obtained directly from Euler computations for a vortex–nozzle interaction with a flow Mach number of 0.01 are shown in figure 15 (time non-dimensionalized by S_1/U_1, change in pressure by $\frac{1}{2}\rho_1 U_1^2$). For each computation, the vortex was generated with its core positioned 0.4 times the height of the channel above the lower wall, and had a final circulation of -1.5 (non-dimensionalized by $U_1 S_1$). The portion of the responses shown is that after the generation of the vortex.

The differences between the coarse- and fine-mesh results arise mostly due to their relative differences in discretization errors associated with the transport of vorticity over extended distances. In general, the coarse mesh was less able to maintain the magnitude and distribution of vorticity in the core region as the vortex was convected from its generation point to the nozzle. Discretization errors associated with the propagation of the acoustic wave are also greater for coarser meshes, but these are relatively small for the wavelengths being considered. In separate tests performed

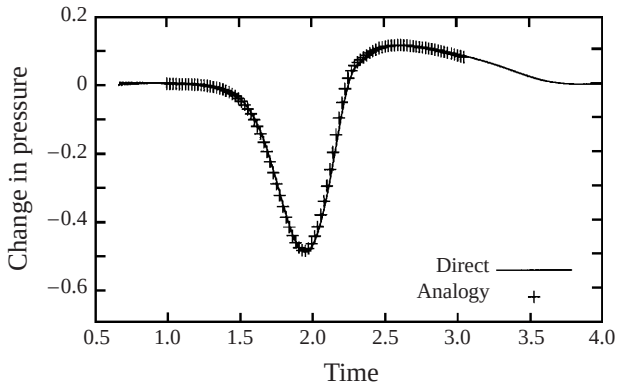

FIGURE 16. Upstream pressure perturbations measured directly from a fine-mesh Euler computation compared with the perturbation obtained indirectly with (2.6) using a volume integration of the computed Euler solution ($M_1 = 0.01$, $\Gamma = -1.5$, $h = 0.4$).

with the numerical method, it was found that acoustic waves can be propagated with less than 0.1% amplitude error per wavelength travelled provided a discretization of more than 50 cells per wavelength is maintained. The discretization of the coarse mesh is well in excess of this for both the longitudinal and transverse components of the acoustic response.

In figure 16, an estimation for the upstream perturbation based on (2.6) is compared with the perturbation measured directly from the fine-mesh computation. The integral was evaluated in the volume between two channel widths forward and one channel width aft of the throat, using the computed evolving vorticity distribution. The portions of the signals shown corresponds to those for which the vortex was completely contained by the volume. The good agreement of the signals also suggests that wave propagation errors are small. Overall, the favourable agreement between coarse and fine meshes, and between both methods for determining far-field upstream responses, suggests that the discretization errors present within the fine-mesh results are acceptably low.

In figure 17, the directly measured fine-mesh Euler signal is compared with that computed using the vortex-blob method, interpreted with (2.6). The vortex-blob calculation was initiated using a 237 point-vortex approximation to the $M_1 = 0.01$ fine-mesh Euler vorticity distribution at $t = 0.7$. The vorticity distributions of the two methods are compared at later times in figure 18. In general the response is similar to that computed directly from the Euler solution. The comparison is again favourable considering that the two methods have completely different sources of error.

3.4. *The effect of increasing Mach number*

Upstream pressure perturbations determined directly from Euler computations are shown for a range of subcritical Mach numbers in figure 19. In all cases, the vortices generated upstream had similar values of non-dimensionalized circulation, although their initial vorticity distributions were not identical due to variations in vortex generation with convection velocity. Also shown in each plot is the upstream pressure perturbation determined using the vortex-blob technique, initiated using equivalent point-vortex distributions.

The character of the directly measured Euler signal changes in a number of ways as the Mach number is increased. First, there is an overall increase in the amplitude of

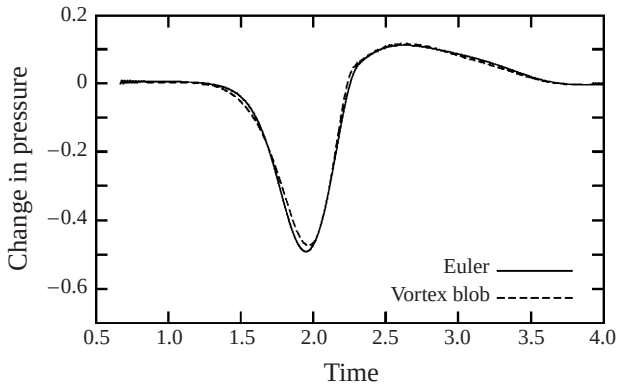

FIGURE 17. Comparison of the directly determined Euler perturbation and the perturbation determined using the vortex-blob method initialized with the Euler vorticity field ($M_1 = 0.01$, $\Gamma = -1.5$, $h = 0.4$).

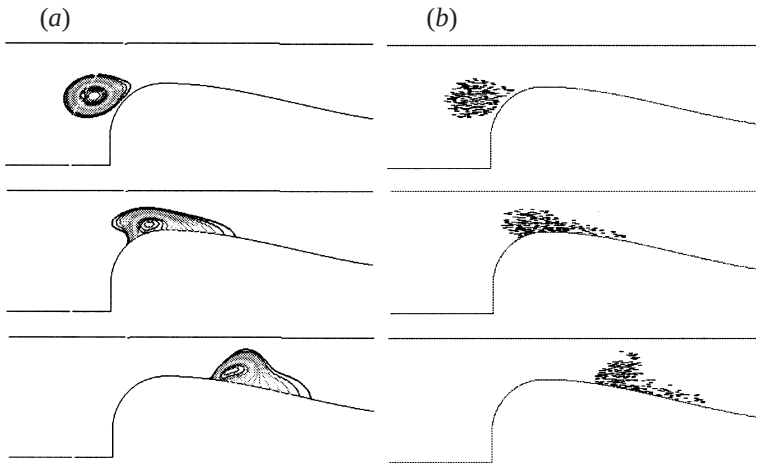

FIGURE 18. Comparison of vorticity magnitude contours from the Euler computation (*a*) and vortex blob positions (*b*) at $tU/S = 1.7$, 2, and 2.3 ($M_1 = 0.01$, $\Gamma = -1.5$, $h = 0.4$).

the signal. Secondly, a small maximum develops before the main dip, which increases relative to the remainder of the response with increasing Mach number. Thirdly, the time scale of the aft portion of the signal is significantly increased. Finally, a superimposed excitation, corresponding in frequency to the first transverse mode of the upstream channel, appears on the aft portion of the signal, with an amplitude increasing with Mach number.

In contrast, only the increase in signal amplitude is observed in the results computed using the vortex-blob technique (This effect can be anticipated by considering the Doppler factors $(1-M_1)$ and $(1-M_2)$ appearing in (2.6)). As the vortex-blob method makes no computation of local Mach number, an estimate for the local retarded time cannot be made. Thus it is unable to predict the increasing delay of the aft part of the signal which arises due to the increasing throat Mach number. Finally, as the expression (2.6) is based on the assumption of a plane propagating wave, it does not allow representation of the oscillations corresponding to transverse mode excitations observed in the Euler solution.

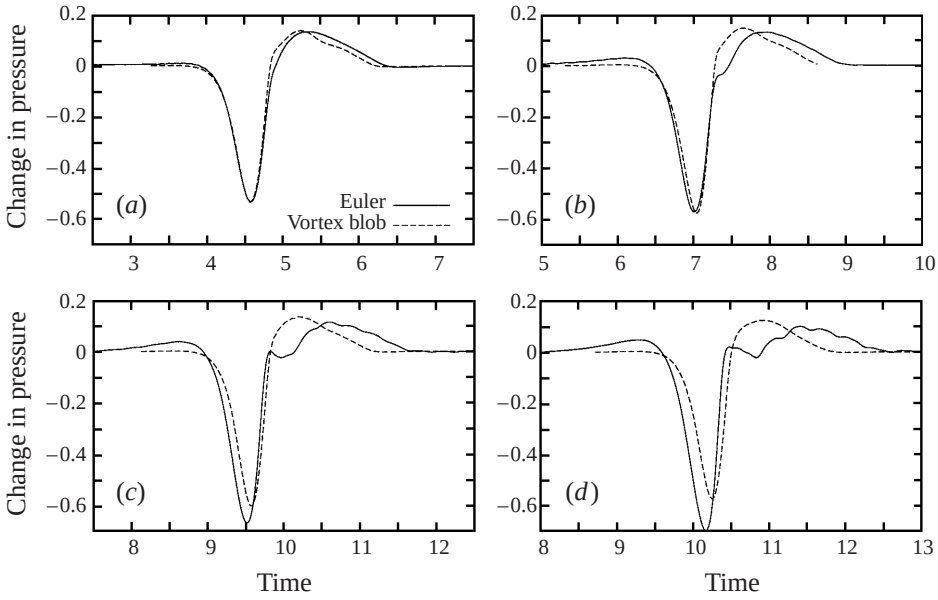

FIGURE 19. Comparisons of Euler and vortex-blob computed perturbations for (*a*) $M_1 = 0.05$, (*b*) 0.10, (*c*) 0.15, and (*d*) 0.175 ($\Gamma = -1.5$, $h = 0.4$).

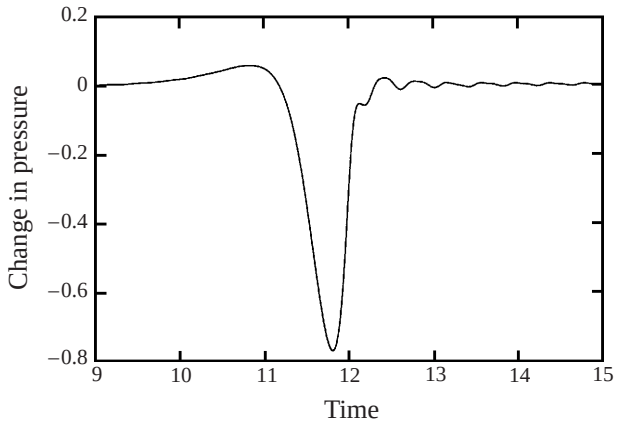

FIGURE 20. Euler computation of upstream pressure perturbation in choked conditions ($M_1 = 0.196$, $\Gamma = -1.5$, $h = 0.4$).

3.5. *Choked conditions*

The upstream pressure perturbation due to the convection of a vortex through a nozzle operating at choked conditions appears in figure 20. The circulation of the vortex was similar to that considered in the previous subcritical cases. Instead of an anechoic condition at the outflow boundary of the domain, however, a constant pressure was approximately maintained by specifying variable-strength incoming waves proportional to the local deviation from the required pressure. This allowed a sonic throat to be maintained during the passage of the vortex through the nozzle.

The choked condition is characterized by the complete disappearance of the aft maximum. As the vortex enters through the throat, it momentarily distorts the sonic

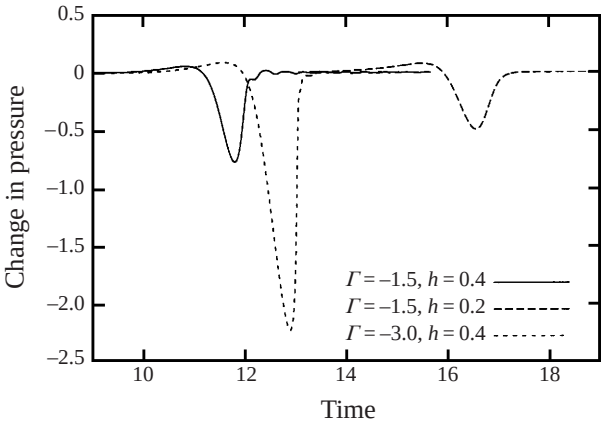

FIGURE 21. Euler computation of upstream pressure perturbation in choked conditions for varying circulations and initial heights ($M_1 = 0.196$).

line, and then passes through it. Afterwards, the sound generation of the vortex is cut off, leaving only the oscillations arising due to transverse mode excitation.

Results for varying vortex height and circulation are shown in figure 21. These give similar effects to those observed for low Mach numbers, including the signal retardation and nonlinear dependence of amplitude on circulation.

3.6. *Bifurcations*

In § 2.3, it was shown that for high values of circulation and low initial heights, it is possible for a point vortex to become confined within a simple rectangular nozzle domain. This type of solution bifurcation has also been observed with distributed vorticity and geometrically smooth nozzles. Figure 22 shows vorticity magnitude plots for two vortices with a relatively large initial circulation of $\Gamma = -3.0$ interacting with a choked nozzle. The first of these (left), was generated at a height of of $h = 0.4$ and produced the third signal shown in figure 21. Due to its high circulation, the vortex is drawn closer to the lower throat surface, resulting in a stretched vorticity distribution. The basic character of response, however, is unchanged from that of the $\Gamma = -1.5$ case.

In contrast, the $\Gamma = -3.0$ vortex released at $h = 0.2$ becomes only partially stretched in the direction of the throat, while most of its vorticity remains trapped in the corner of the geometry. (Note that the $h = 0.2$ vortex has initially more widely distributed vorticity than the $h = 0.4$ case due to interactions with the lower wall during the generation process.)

The resulting upstream perturbations are compared in figure 23. The $h = 0.2$ vortex shows a marked reduction in the minimum pressure peak, as most of the vorticity does not pass through the throat. The pressure minimum is followed by a low-frequency oscillation, corresponding to the oscillation of the vortex core in the corner region.

The pulsations occurring in solid-rocket motors do not seem to include lower hydrodynamic modes. The main reason for their absence is expected to be the stabilizing effect of confinement on modes with a large wavelength compared to the channel height. Bifurcations of the type described above, however, may also provide an additional explanation. The lowest mode observed in Dotson *et al.* (1997) corresponds to five vortices between the vortex generation point (a discontinuity in the rocket propellant) and the nozzle. The presence of less than five vortices would

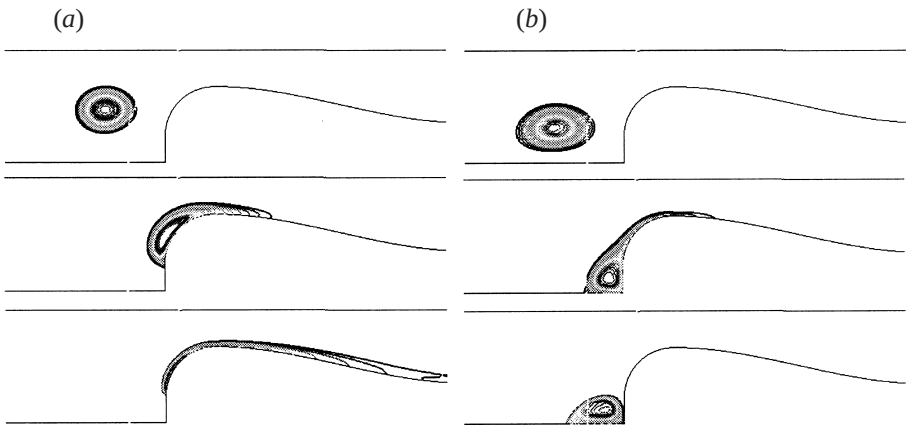

FIGURE 22. Comparison of vorticity magnitude contours from two Euler computations with equivalent initial vortex circulations but different initial heights ($M_1 = 0.196$, $\Gamma = -3.0$; (*a*) $h = 0.4$, (*b*) $h = 0.2$).

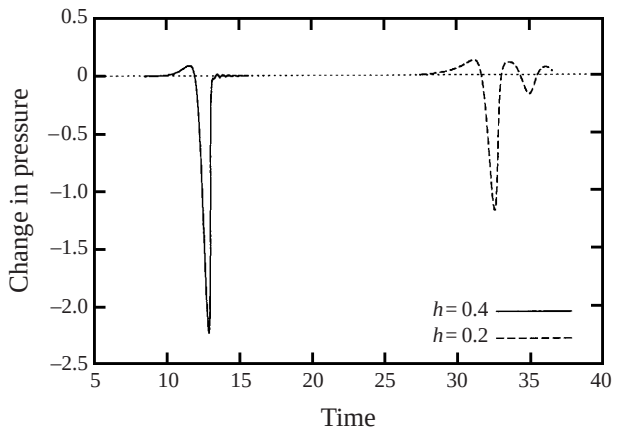

FIGURE 23. Euler computation of upstream pressure perturbation in choked conditions from two Euler computations with equivalent initial vortex circulations but different initial heights ($M_1 = 0.196$, $\Gamma = -3.0$).

imply larger values of circulation, which may prevent the individual ingestion of the vortices by the nozzle. In the data of Dotson *et al.* a change to a lower acoustic mode is finally observed when there are twelve vortices. This is expected to occur due to the merging of these relatively weak vortices before the nozzle is reached.

4. Conclusion

We have considered the sound production of inviscid vortex–nozzle interactions at both low and high Mach numbers, with the goal of characterizing the most important factors that influence them. The results have implications for the construction of approximate models used to predict solid-rocket motor pulsations.

The most important factors influencing the magnitude and phase of sound production at low Mach numbers are the vortex circulation and its initial position. The detailed geometry of the nozzle and the distribution of vorticity also play impor-

tant roles in determining the precise form of the signal. It was confirmed that the vortex-sound analogy for compact source regions developed by Howe, combined with a simulation of incompressible vorticity dynamics introduced by Powell (referred to here as the Powell–Howe analogy), can be used to accurately predict sound production for nozzles operating at low Mach numbers. In fact, for smooth nozzles, a single point vortex may be used to estimate the most important effects influencing sound production.

At the higher operating Mach numbers typical of solid-rocket nozzles, the sound production becomes significantly influenced by the non-compactness of the source. This partly manifests itself as an increase in the time scale of the second half of the signal, generated after the vortex enters the nozzle throat. The lengthening and gradual attenuation of the second half of the signal appears to transition smoothly to the result for choked conditions, where it disappears completely. An additional effect observed at higher Mach numbers is the increasing pressure amplitudes in the initial portions of the signal. These have been found to be in excess of the increases predicted by the Doppler factors present in (2.4).

The importance of non-compact source effects and mean-flow compressibility at higher Mach numbers means that the Powell–Howe analogy cannot be used to predict all features of vortex sound generation in rocket-nozzle flows. From the point of view of estimating the order of pulsation amplitudes, however, an acceptable approximation might be obtained by truncating the signal obtained from the Powell–Howe analogy after the vortex enters the throat region. This would be particularly applicable for nozzle geometries which feature complex curvatures before the throat, for which much of the sound generation is in the low Mach number region.

Finally, the study has shown that under conditions with large values of vortex circulation, a solution bifurcation occurs. In such cases, the vortex may be partially repelled from the nozzle. This effect may help to explain why only higher hydrodynamic modes are observed in solid-rocket motors, as it precludes ingestion of the large-circulation vortices that would be present in a lower-order pulsation.

Part of this work was carried out while S. J. H. was at the Department of Mechanical Engineering, University of Twente, The Netherlands.

REFERENCES

Anthoine, J., Buchlin, J.-M. & Guery, J.-F. 2000 Experimental and numerical investigations of nozzle geometry effect on the instabilities in solid propellant boosters. *AIAA Paper* 2000-3560.

Anthoine, J., Olivari, D., Hulshoff, S. J. & Van Rooij, M. 1998 Qualitative model of vortex-induced oscillations in a model of solid propellant boosters. *AIAA Paper* 98-2270.

Brown, C. E. & Micheal, W. H. 1954 Effect of leading-edge separation on the lift of a delta wing. *J. Aero. Sci.* **21**, 690–694.

Bruggeman, J. C., Hirschberg, A., Dongen, M. E. H. van, Wijnands, A. P. J. & Gorter J. 1991 Flow induced pulsations in gas transport systems: analysis of the influence of closed side branches. *J. Sound Vib.* **150**, 371–393.

Conlisk, A. T. & Rockwell, D. 1981 Modeling of vortex-corner interaction using point vortices. *Phys. Fluids* **24**, 2133–2142.

Couton, D., Plourde, F., Vetel, J. & Doan-Kim, S. 1998 Le couplage aero-acoustic et sa caracterisation sur un montage en gaz froid - MICAT-1. *3e Colloque R&D "Ecoulements Internes en Combustion Solide" ONERA/CNES/ENSMA, Poitiers, France, 25–27 March* (ed. Y. Fabignon).

Doan Kim, M. S., Plourde, F. & Couton, D. 1997 Simulation en gaz froid/ montage MICAT-1", rapport final. ENSMA/LET N^o RA 2/97 axe "SF", Ecole Nationale Supérieure de Mécanique et d'Aérotechnique, Poitiers, France.

Dotson, K. W., Koshigoe, S. & Pace, K. K. 1997 Vortex shedding in a large solid rocket motor without inhibitors at the segments interfaces. *J. Propulsion Power* **13**, 197–206.

Dunlap, R. & Brown, R. S. 1981 Exploratory experiments on acoustic oscillations driven by periodic vortex shedding. *AIAA J.* **19**, 408–409.

Dunne, R. C. & Howe, M. S. 1997 Wall-bounded blade-tip vortex interaction noise. *J. Sound Vib.* **202**, 597–610.

Flandro, G. A. 1986 Vortex driving mechanism in oscillatory rocket flows. *J. Propulsion* **2**, 206–214.

Graziani, G., Ranucci, M. & Piva, R. 1995 From a boundary integral formulation to a vortex method for viscous flows. *Comput. Mech.* **15**, 301–314.

Hirschberg, A., Hulshoff, S., Hassel, R. R. van & Anthoine, J. 1998 Vortex-acoustic interaction in internal flows: the Whistler-nozzle, human whistling, and the solid-propellant rocket motor. *3e Colloque R&D "Ecoulements Internes en Combustion Solide" ONERA/CNES/ENSMA, Poitiers, France, 25–27 March* (ed. Y. Fabignon).

Hofmans, G. C. J. 1998 Vortex sound in confined flows. PhD Thesis, Technische Universiteit Eindhoven.

Hourigan, K., Welsh, M. C. & Thompson, M. C. 1990 Aerodynamic sources of acoustic resonance in a duct with baffles. *J. Fluids Struct.* **4**, 345–370.

Howe, M. S. 1975*a* The generation of sound by aerodynamic sources in inhomogeneous steady flow. *J. Fluid Mech.* **67**, 597–610.

Howe, M. S. 1975*b* Contributions to the theory of aerodynamic sound, with application to excess jet noise and the theory of the flute. *J. Fluid Mech.* **71**, 625–673.

Howe, M. S. 1998 *Acoustics of Fluid-Structure Interactions.* Cambridge University Press.

Hulshoff, S. J., Hoeijmakers, H. W. M. & Mulder, J. A. 1996 Prediction of aircraft longitudinal response using time-accurate Euler computations. *AIAA Paper* 96-2485.

Krasny, R. 1987 Computation of vortex sheet roll-up in the Treffetz plane. *J. Fluid Mech.* **184**, 123–155.

Lighthill, M. J. 1954 On sound generated aerodynamically II. *Proc. R. Soc. Lond.* A **222**, 1–32.

Peters, M. C. A. M. 1993 Aeroacoustic sources in internal flows. PhD Thesis, Technische Universiteit Eindhoven.

Poinsot, T., J. & Lele, S. K. 1992 Boundary conditions for the direct simulation of compressible viscous flows. *J. Comput. Phys.* **101**, 104–129.

Powell, A. 1964 Theory of vortex sound. *J. Acoust. Soc. Am.* **36**, 177–195.

Thompson, K. W. 1987 Time-dependent boundary conditions for hyperbolic systems I. *J. Comput. Phys.* **68**, 1–24.

Thompson, K. W. 1990 Time-dependent boundary conditions for hyperbolic systems II. *J. Comput. Phys.* **89**, 439–461.

Thompson, M. C., Hourigan, K. & Welsh, M. C. 1992 Acoustic sources in a tripped flow past a resonator tube. *AIAA J.* **30**, 1484–1491.

Vuillot, F. 1995 Vortex-shedding phenomena in solid rocket motors. *J. Propulsion Power* **11**, 626–639.